Science of the Total Environment 757 (2021) 143717

Contents lists available at ScienceDirect

Science of the Total Environment

journal homepage: www.elsevier.com/locate/scitotenv

Unveiling the correlation of Fe_3O_4 fractions upon the adsorption behavior of sulfamethoxazole on magnetic activated carbon

Miao Lv [a,1], Dongyi Li [b,1], Zhaohan Zhang [a,*], Bruce E. Logan [c], Guohong Liu [a], Muchen Sun [a], Changchao Dai [a], Yujie Feng [a,*]

[a] State Key Laboratory of Urban Water Resource and Environment, School of Environment, Harbin Institute of Technology, Harbin 150090, China
[b] School of Environmental Science and Engineering, Tianjin University, No. 92 Weijin Road, Nankai District, Tianjin 300072, China
[c] Department of Civil and Environmental Engineering, Penn State University, 212 Sackett Building, University Park, PA 16802, United States

HIGHLIGHTS

- The monolayered MPs uniformly grew on the surface of PAC.
- MPs loading ratios will trade-off between magnetism and adsorption capacity.
- The formed (−)CAHB was responsible for SMX^- adsorption on MPAC.
- MPAC was suggested as efficient and sustainable adsorbent for SMX removal.

GRAPHICAL ABSTRACT

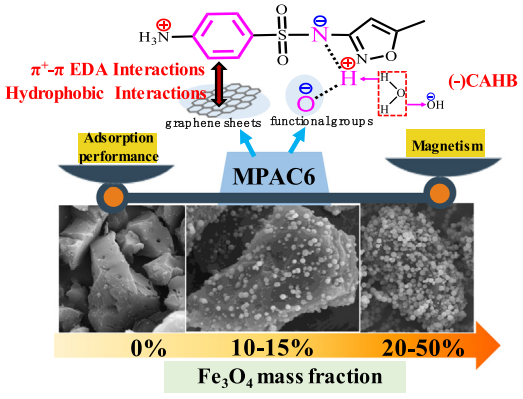

ARTICLE INFO

Article history:
Received 16 May 2020
Received in revised form 28 October 2020
Accepted 9 November 2020
Available online 14 November 2020

Editor: Baoliang Chen

Keywords:
Adsorption
Magnetic activated carbon
Sulfamethoxazole
Isotherm
Regeneration

ABSTRACT

Magnetic particles (MPs) assisted powdered activated carbon (PAC) is a promising composite material for adsorption removal of micropollutants. The fractional amount of Fe_3O_4 impacts the balance between adsorption capacity and magnetic property of magnetic activated carbons (MPACs), and therefore it affects the extent of sulfamethoxazole (SMX) removal. Here, five MPACs with different mass ratios of Fe_3O_4: PAC (1:1, 1:2, 1:4, 1:6, and 1:8) were prepared using a hydrothermal method and characterized by various spectroscopic methods. The spherical shaped MPs were monolayerly deposited on PAC with fewer pores blocked when the mass ratio of Fe_3O_4 was comparatively low (≤ 20%). MPAC6 (14.3 wt% of Fe_3O_4) had the best overall performance, with good Langmuir adsorption capacities for SMX (173.0 mg g^{-1}) and excellent magnetic properties (9.0 emu g^{-1}). Corresponding adsorption kinetics fitted well with the pseudo second-order kinetic model. The negative ΔG^0 (−25.6 to −27.2 KJ mol^{-1}) and ΔH^0 (−9.14 KJ mol^{-1}), and positive ΔS^0 (0.55 KJ mol^{-1} K^{-1}) properties indicated the spontaneous and exothermic nature of the adsorption process accompanied by an increase in entropy. The strong cation-assisted electron donor-acceptor and hydrophobic interactions were contributed to a high extent of SMX removal in the pH range of 2–4. Formation of negative charge-assisted H-bonds was responsible for the adsorption of hydrophilic SMX^- on negatively charged MPAC6 in alkaline solution. Desorption and regeneration experiments showed SMX removal was still 92.3% in the 5th cycle. These findings give valuable insights into the interactions between SMX and MPACs and guide for choosing sustainable magnetic adsorbents for environmental applications.

* Corresponding authors.
E-mail addresses: hitzzh@hit.edu.cn (Z. Zhang), yujief@hit.edu.cn (Y. Feng).
[1] These authors contributed equally to this work and should be considered co-first authors.

https://doi.org/10.1016/j.scitotenv.2020.143717
0048-9697/

1. Introduction

Sulfamethoxazole (SMX) is an antibiotic that is widely used in human and veterinary pharmaceuticals to prevent and treat diseases (Straub, 2016; Liu et al., 2017a). In China, 313 tons of SMX were produced for human and animal use in 2013, and a large fraction of it was discharged into the environment due to its poor degradation in the wastewater treatment plant (WWTP) (Zhang et al., 2015). SMX is one of the most frequently detected antibiotics in surface waters and wastewaters (Wei et al., 2011), and long-term exposure of SMX could induce antibiotic-resistance to pathogens and be toxic to aquatic organisms (Gao et al., 2012; Sun et al., 2020). Moreover, the continuous release of SMX increased the possibility of bioaccumulation and biomagnification of SMX in aquatic organisms and eventually be transmitted to humans through the food chain (Liu et al., 2017b). Thus, it is of great importance to remove SMX from the water before discharging into aquatic environments.

Commonly used techniques for SMX removal include adsorption, membrane filtration, ion exchange, and advanced oxidation processes (Pamphile et al., 2019; Bao et al., 2018; Tong et al., 2017; Tang and Wang, 2018). Among them, adsorption is considered to be the most competitive method because it is relatively inexpensive and it can be easily implemented in large-scale applications without generating undesired oxidation-derived products (Heo et al., 2019). Activated carbon (AC) is an effective adsorbent for organic pollutants removal due to its high surface area, rich porous structure, excellent stability, and diverse surface functional groups (Zhang et al., 2016). Powdered activated carbon (PAC) is superior to granular activated carbon (GAC) for adsorption due to its larger surface area per mass of material (Gong et al., 2016; Altmann et al., 2014). PAC is an extremely versatile material that can adsorb a wide range of organic micro-pollutants, such as endocrine-disrupting chemicals, pharmaceuticals, and personal care products (Zietzschmann et al., 2016; Joseph et al., 2013; Kaur et al., 2018). However, a major drawback for practical applications of PAC is the difficulty of efficiently separating PAC from aqueous solutions after treatment due to its small size.

The magnetization of PACs by jointing the adsorbent with magnetic particles has been confirmed to be an efficient and promising approach to collect PACs (Rezaei Kalantary et al., 2016; Rezaei Kalantry et al., 2016). The high-speed recovery of magnetic activated carbons (MPACs) from the treated water can be attained by applying an external magnetic field, avoiding inefficient and costly coagulation, filtration, and centrifugation processes. MPACs have therefore been widely employed as economic, efficient, and eco-friendly adsorbents for organic contaminants removal. Some studies have recently reported on using magnetic carbon composites for sulfonamides removal. Wan et al. measured 27% lower SMX adsorption capacity of MPAC compared to PAC (159 mg g^{-1} vs. 217 mg g^{-1}) and attributed this to the 26% reduction in the surface area (652 m^2 g^{-1}vs. 875 m^2 g^{-1}), although the reduction might also have originated from the lower PAC mass fraction in the MPAC (Wan et al., 2014). Reguyal et al. synthesized the magnetic biochar that had 21% reduced SMX adsorption capacities than pristine biochar (13.8 mg g^{-1} vs. 17.5 mg g^{-1}), while its surface area was 58% lower than that of the pristine biochar (125.8 m^2 g^{-1} vs. 297.8 m^2 g^{-1}) with 27% less C mass fractions (Reguyal et al., 2017). In contrast, Zhang et al. reported the SMX adsorption capacity of prepared magnetic biochar was 5.3 times higher than the pristine biochar (Zhang et al., 2020). Therefore, it is still unclear how MPs influence the adsorption behavior of MPACs. Our understandings of the links between the surface area, activated carbon content and the adsorption capacities of pollutants on MPACs are still developing. A systematic study evaluating the adsorption behavior of MPACs with varying mass fractions of MPs is vital for the elaboration of the separate contributions of MPs and PAC on MPACs.

To guide the optimization of the magnetic adsorbent regarding magnetic separation while minimizing interference on pollutants adsorption capacity, the objectives of this study were to: (i) prepare and characterize the MPACs containing different mass fractions of MPs; (ii) investigate the effects of the pH, ion species/strength, and natural organic matter (NOM) on the adsorption of SMX; (iii) illuminate the influence of MPs in the adsorption behavior and mechanisms of SMX on MPACs; (iv) determine the regeneration extent and durability of MPACs. Obtaining such information can provide a more theoretical and technological basis for producing more efficient magnetic adsorbents for SMX removal.

2. Materials and methods

2.1. Materials

Powder activated carbon was purchased from Benchmark Instrument (Tianjin, China). Ferric chloride ($Fe_3Cl_6{\cdot}6H_2O$, 99%), sodium acetate (NaOAc, 99%), polyethylene glycol (PEG2000, 99%), and ethylene glycol (EG) were obtained from Sinopharm (Beijing, China) and used for Fe_3O_4 preparation. Sulfamethoxazole (SMX, 99%) was purchased from Sigma-Aldrich (St. Louis, MO). The molecular structure and physicochemical properties of SMX are summarized in Fig. S1 and Table S1. Acetonitrile and formic acid were HPLC grade and obtained from Fisher Chemicals (Fair Lawn, NJ, USA). All chemicals were used as received without any further treatment. In all cases, deionized water was used to prepare the solutions.

2.2. Preparation of MPACs

MPACs nanocomposites were prepared based on a facile hydrothermal method (Deng et al., 2005). Different amounts of PAC were dispersed in EG (60 mL) by ultrasonication for 30 min at room temperature (25 °C). Then, $Fe_3Cl_6{\cdot}6H_2O$ (2.03 g, 7.5 mM) was dissolved in the PAC solution, followed by the addition of NaOAc (4.9 g) and PEG (1.0 g). The mixture was stirred vigorously for 60 min, sealed in a Teflon-lined stainless-steel autoclave (100 mL) which was heated at 200 °C for 8 h, and then cooled to room temperature. The obtained products were washed six times with ethanol and ultrapure water, dried at 60 °C for 8 h in the vacuum drying oven, and grinded into powder for experiments. A series of mass ratios of Fe_3O_4: PAC were tested of 1:1, 1:2, 1:4, 1:6, and 1:8 (designated as MPAC1, MPAC2, MPAC4, MPAC6, and MPAC8, respectively) to investigate the influence of MPs in the adsorption behavior of SMX on MPACs.

2.3. Characterization of MPACs

The morphologies of the prepared MPACs were characterized by scanning electron microscope (Sigma500, Zeiss, Germany) operating at an accelerating voltage of 10 kV, which was equipped with an Oxford Link X-Max 50 energy dispersion spectrometry (Oxford Instruments, UK) for elemental mapping analysis. Powder X-ray diffraction (XRD) patterns were acquired with a D8 advance X-ray diffractometer (Bruker, Germany) using Cu Ka radiation (40 kV, 300 mA) from 10° to 90°. The crystal sizes of samples were calculated from the strongest peak (311) according to the Debye-Scherrer's formula $D = K\lambda/(\beta\cos\theta)$ (Li et al., 2010), where $K = 0.94$ is a dimensionless constant for a cubic structure, $\lambda = 0.154$ nm the wavelength of X-ray radiation, β the full width at half maximum (FWHM) of the peak (311), and θ the Bragg's diffraction angle. The magnetic properties were measured using a vibrating sample magnetometer (VSM, Lake Shore 7404, USA). The Brunauer–Emmett–Teller (BET) surface area was analyzed with Micromeritics ASAP 2020 surface area and porosity analyzer with N_2 gas (Quantachrome, USA). The precise carbon content in the magnetic composites was determined by a Vario EL cube elemental analyzer (Elementar, Germany). Zeta potentials were measured using a Zetasizer 2000 (Malvern, UK). Thermal gravimetric analysis (TGA) was measured in the nitrogen flow with a PerkinElmer Thermal Analyzer at a heating rate of 10 °C min^{-1}. FTIR

spectra were recorded in the region of 4000–400 cm^{-1} on a Perkin-Elmer Spectrum One FTIR spectrometer (Perkin-Elmer, USA). The elemental compositions and their chemical states of the adsorbents were determined through the X-ray photoelectron spectroscopy (XPS, PHI 5700 ESCA System, USA) with an Al Kα source (1486.6 eV, 10 mA 15 kV).

2.4. Adsorption experiments designs

Batch adsorption experiments were conducted on a model KYC-1102C thermostat shaker (Ningbo, China) at 150 rpm. The SMX solutions (0.6 mg L^{-1}, 50 mL) with 5 mg of adsorbents were placed in stoppered conical flasks and shaken at 25 °C for 60 min unless otherwise noted. The background solutions were prepared by 0.01 M NaCl to maintain constant ionic strength. For kinetic studies, the residual SMX was measured after adsorption times of 1, 2, 3, 4, 5, 6, 7, 8, 9, 10, 12, 15, 20, 25, 30, 45, and 60 min. The sorption isotherm experiments were conducted at the initial concentrations of SMX ranging from 0.5 to 50 mg L^{-1} at 25 °C for 180 min. The adsorption thermodynamics were investigated at three temperatures of 25 °C, 35 °C, 45 °C, and 55 °C with varying initial concentrations.

Single-point adsorption experiments were conducted to investigate the effects of pH, ion species/strength, and natural organic matter (NOM) on the adsorption of SMX. The initial pH values were adjusted to 2–12 by 0.1 M HCl or NaOH. Five different ions, i.e., SO_4^{2-}, Cl^-, NO_3^-, PO_4^{3-}, and NH_4^+ were selected as representative ions in real water. The ion concentration of 0–0.5 M and NOM (humic acid) concentration of 0–10 mg L^{-1} were applied. SMX solutions were filtered with 0.45 μm membranes and analyzed using an ultra-performance liquid chromatography (UPLC) system (Waters, Milford MA) equipped with a UV absorbance detector. An ACQUITY UPLC BEH C18 column (130 Å, 1.7 μm, 1 mm × 100 mm; Waters) was used for analytes separation. The two eluents were a 70:30 mixture of ultra-pure water with 0.1% formic acid (v/v) and acetonitrile at a total flow rate of 0.1 mL min^{-1}. The detection wavelength for SMX was 260 nm, and the limit of quantitation was 10 μg L^{-1}.

Desorption experiments were conducted to evaluate the regeneration characteristics of MPAC6. MPAC6 (5 mg) was added to 50 mL SMX solution (25 mg L^{-1}) with a contact time of 60 min. After adsorption, the separated MPAC6 was treated by four regeneration methods including (i) acid washing; (ii) alkaline washing; (iii) ethanol washing; and (iv) thermal treatment. For the first three methods, the adsorbents were each placed into conical flasks containing 10 mL of 0.1 M HCl, 0.1 M NaOH, and ethanol, shaken for 60 min, separated from the suspension, and then dried at 60 °C for 2 h. For the thermal regeneration test, the adsorbents were heated at 350 °C for 2 h in a tubular furnace with a continuous flow of N_2. Five sequential cycles of adsorption-desorption were carried out to evaluate the recycling performance.

2.5. Calculations

The adsorption kinetics were fitted to describe the solid phase mass loading of SMX with pseudo-first-order ($Q_{t,1}$) (Jiang et al., 2017), pseudo-second-order ($Q_{t,2}$) (Zhu et al., 2011a), intraparticle diffusion ($Q_{t,diff}$) (Fan et al., 2012), and Elovich ($Q_{t,e}$) (Kakavandi et al., 2016) kinetic models. The three models were:

$$Q_t = Q_e\left(1-e^{-k_1 t}\right) \tag{1}$$

$$Q_t = \frac{Q_e^2 k_2 t}{1+Q_e k_2 t} \tag{2}$$

$$Q_t = \frac{1}{\beta}\ \ln(1+\alpha\beta t) \tag{3}$$

$$Q_t = k_{diff} t^{0.5} + C \tag{4}$$

where Q_t (mg g^{-1}) is the solid-phase loading of SMX at the adsorbent time t (min), Q_e (mg g^{-1}) the adsorption capacity at equilibrium, k_1 (min^{-1}) the first-order rate constant, k_2 (g mg^{-1} min^{-1}) the second-order rate constant, k_{diff} (mg g^{-1} $min^{-0.5}$) the intraparticle diffusion rate constant, C (mg g^{-1}) a constant that indicated the thickness of boundary layer (Valderrama et al., 2008), α (mg g^{-1} min^{-1}) the initial adsorption rate, and β (g mg^{-1}) the desorption constant.

Adsorption data were fit by the Langmuir adsorption ($Q_{e,L}$), Freundlich ($Q_{e,F}$), Temkin ($Q_{e,T}$), and Dubinin-Radushkevich models ($Q_{e,DR}$) using:

$$Q_{e,L} = \frac{Q_{Lmax} K_L C_e}{1+K_L C_e} \tag{5}$$

$$Q_{e,F} = K_F C^{1/n} \tag{6}$$

$$Q_{e,T} = \frac{RT}{b_T}\ \ln(K_T C_e) \tag{7}$$

$$Q_{e,DR} = Q_{DRmax}\ \exp\left[-K_{DA}\left(RT\ln\left(\frac{C_s}{C_e}\right)\right)\right]^2 \tag{8}$$

where Q_{Lmax} (mg g^{-1}) is the maximum adsorption capacity calculated from the Langmuir model, K_L (L mg^{-1}) the Langmuir constant, C_e (mg L^{-1}) the aqueous equilibrium concentration of SMX, K_F [(mg g^{-1}) (L $mg^{-1})^{1/n}$] the Freundlich constant, 1/n the Freundlich adsorption intensity parameter, b_T the Temkin constant related to the adsorption heat (J g mol^{-1} mg^{-1}), K_T the Temkin equilibrium binding constant (dm^3 mg^{-1}), Q_{DRmax} the maximum adsorption capacity calculated from Dubinin-Radushkevich model (mg g^{-1}), C_s monolayer saturation concentration of adsorbate (mg L^{-1}), K_{DR} the isotherm constant related to the sorption energy (mol^2 kJ^{-2}).

The standard Gibbs free energy change (ΔG^0), enthalpy change (ΔH^0), and entropy change (ΔS^0) were determined using:

$$\Delta G^0 = -RT\ln K_a \tag{9}$$

$$\Delta G^0 = \Delta H^0 - T\Delta S^0 \tag{10}$$

$$\ln K_a = -\frac{\Delta H^0}{RT} + \frac{\Delta S^0}{R} \tag{11}$$

where K_a is the thermodynamic equilibrium constant without units, T (K) is the operating temperature in Kelvin, R is the gas constant with a value of 8.314 J mol^{-1} K^{-1}, and ΔH^0 and ΔS^0 were obtained from the slope and intercept of the linear plot of ln K_a versus 1/T (Liu and Xu, 2007).

3. Results and discussion

3.1. Characterization of adsorbents

Elemental analysis was employed to characterize the chemical compositions of the adsorbents. The amounts of C and H decreased with the increased Fe_3O_4 fractions in MPACs (Table 1). This result is expected since PAC could be the only source of C and H and Fe_3O_4 could be the main source of Fe in the MPACs. The N% for all adsorbent was very low (<0.42%). The O content in the MPACs could be derived from both PAC and Fe_3O_4, which could not be obtained by mass difference. The ash content of PAC was very low (2.6%). The ash content of the MPACs was not measured because the residuals of iron oxide after the combustion of magnetic carbons could lead to significant errors.

The results of the N_2 adsorption/desorption showed that the surface area was reduced from 2040 m^2 g^{-1} to 665–1230 m^2 g^{-1} based on different ratios of MPs impregnating the PACs (Table 1). The reduction of the surface area of carbonaceous adsorbents by the addition of MPs has been reported in the previous studies. Based on IUPAC classification,

Table 1
The textural properties of adsorbents.

Adsorbents	C (%)	H (%)	N (%)	O[a] (%)	Fe[b] (%)	PAC (%)	S_{B-E-T} (m^2g^{-1})	V ($cm^3\ g^{-1}$)	D_{BJH} (nm)
PAC	92.2	1.67	0.42	5.91	–	100	2040	0.47	2.83
MPAC1	47.8	0.82	<0.3	–	46.4	51.2	387	0.19	3.22
MPAC2	59.9	0.95	<0.3	–	35.9	65.1	428	0.20	3.11
MPAC4	69.2	1.16	<0.3	–	22.4	75.2	498	0.24	3.20
MPAC6	75.4	1.32	<0.3	–	21.3	81.9	794	0.29	2.82
MPAC8	76.8	1.35	<0.3	–	15.5	83.5	1014	0.32	2.88
MPs	–	–	–	–	82.9	0	40	0.15	13.1

[a] O (%) for MPACs could not be obtained by mass difference.
[b] Obtained from EDS results.

N_2 adsorption-desorption isotherms of PAC and MPACs belonged to a hybrid type I and IV, corresponding to porous carbon with hierarchical pore size distribution (Fig. 1). In the case of PAC, significant uptake at low relative pressure was in accordance with the isotherm of type I representing the presence of many micropores (Yang et al., 2018). With the increase of P/P_0 to 0.4–1.0, the isotherms of PAC and MPACs all exhibited type H4 hysteresis loops, which were associated with narrow slit pores and some mesopores (Nguyen et al., 2011). Fe_3O_4 exhibited adsorption features of type III, indicating that magnetic particles were nonporous or macroporous adsorbents with weak affinities. According to the corresponding pore size distribution (Fig. S2), micropores and mesoporous both gradually decreased with an increase in Fe_3O_4 content. Although some pores of the activated carbon were blocked by MPs, these MPACs still retained a large BET surface area and a high pore volume.

The crystalline structures of the prepared materials were further investigated through XRD analysis (Fig. 2a). For pristine PAC, the diffraction profiles exhibited two broad peaks at around 23° and 43° which were assigned to the reflection from (002) and (100)/(101) planes of graphite, indicating the growth of graphite-like microcrystalites on this amorphous carbon (Huang et al., 2015). The MPs had six peaks at 30.1°, 35.5°, 43.2°, 53.6°, 57.1°, and 62.7°, corresponding to (220), (311), (400), (422), (511), and (440) plane of Fe_3O_4 with cubic spinel structure (JCPDS 75–1609), respectively. The peaks of Fe_3O_4 were sharp and intense, indicating their highly crystalline nature. No characteristic peaks of impurities were detected in the XRD pattern. The diffraction peaks appearing in MPACs were indicative of Fe_3O_4 and PAC. Moreover, the observed broader diffraction peaks with increasing carbon loading rates implied that the crystallite sizes of Fe_3O_4 in MPACs gradually decreased. Based on the calculated results, the crystallite sizes of Fe_3O_4 in different materials followed the order of 21.07 nm (Fe_3O_4) > 14.78 nm (MPAC1) > 12.97 nm (MPAC2) > 12.40 nm (MPAC4) > 12.16 nm (MPAC6) > 12.14 nm (MPAC8).

The magnetization curves of Fe_3O_4 and MPACs were measured at 27 °C with an applied magnetic field of ±15 kOe (Fig. 2b). The hysteresis loops of these adsorbents followed a typical super-paramagnetic 'S'-like shape, in which the coercivity and remanence were negligible. The M_s of Fe_3O_4 prepared by the hydrothermal method was 87.4 emu g^{-1}, similar to a previous study (Deng et al., 2005). For MPACs, Ms. values were obtained as 30.1, 17.2, 9.5, 9.0, and 6.1 emu g^{-1}, respectively, performed in the order of decreasing Fe_3O_4 mass proportion from 50% to 11.1%. Do et al. reported that the M_s of xFe_3O_4/PAC (x refers to wt% of Fe_3O_4) were 0.3, 4.7, and 7.0 emu g^{-1} for x = 5, 10, and 30 (Do et al., 2011). For $CuFe_2O_4$/AC magnetic adsorbents with mass ratio of 1:1, 1:1.5 and 1:2, the Ms. were 0.97, 2.30 and 5.93 emu g^{-1} (Zhang et al., 2007). These magnetic properties were good indicators that adsorbents could be easily separated from the solution.

The FTIR spectroscopic analysis in Fig. 2c shows a high-intensity signal for the hydroxyl (—OH) group at 3433 cm^{-1} for Fe_3O_4 and MPAC6, while it is relatively week for PAC. Peaks at 2860 cm^{-1} and 2930 cm^{-1} on PAC and MPAC6 could be ascribed to the stretching vibration of C—H, which came from the characteristic —CH_2— or —CH_3 and indicated the existence of some groups of PAC (Luo et al., 2017). Also, the characteristic peaks in 2376 cm^{-1} and 1506–1540 cm^{-1} due to the stretching vibration of C—C in PAC and MPAC6 confirmed that the carbon was not destroyed in the composite (Ranjithkumar et al., 2014). The peak at 600 cm^{-1} corresponds to the stretching vibration of Fe—O and implies that the presence of iron oxides in the magnetic carbons.

Thermogravimetric analysis of Fe_3O_4, PAC, and magnetic carbons in the nitrogen atmosphere was carried out, with the results shown in Fig. 2d. About 5.4% of mass loss was observed on the TGA curve of Fe_3O_4 at 200–300 °C, while a sharp decrease of PAC weight was obtained at 900 °C. Two steps of mass loss were seen on the TGA curves of MPACs. The first mass loss of MPACs was determined at 300–400 °C and varied irregularly, which might be caused by the evaporation of the adsorbed chemicals during the synthetic process of Fe_3O_4 and MPACs. The second mass loss increased as the increase of carbon content in MPACs, which were attributed to the pyrolysis of PAC. These results indicated that the synthesized magnetic carbons are stable below 900 °C at the nitrogen atmosphere.

As displayed in Fig. 3a, the prepared MPs were spherical shaped, narrowly distributed, and well dispersed, with an average size of 164 ± 14 nm in the diameter. The external surface of raw commercial PAC showed a larger number of pores with various sizes and shapes (Fig. 3c). SEM images of five MPACs demonstrated that the MPs were successfully deposited and randomly distributed on the surface of PAC in the MPACs composites (Fig. 3d–h). Higher loading of MPs led to stacking and forming an irregular crust of MPs on the PAC surface, which could result in PAC pore blockage (Fig. 3d, e). In contrast, the monolayered MPs had uniformly grown on PAC with fewer pores blocked when the MPs content was comparatively low (<20 wt% of Fe_3O_4) (Fig. 3f–h). SEM images of MPAC6 and elemental mappings of carbon (red), oxygen (yellow), and iron (cyan) further confirmed that the homogeneous distribution of MPs on PAC (Fig. 3i–l), based on a brighter area in the elemental map indicating a higher concentration of the corresponding element. The EDS results showed that the compositional ratio of Fe:O was 1:2.3 and the high oxygen content could be attributed to the intrinsic oxygen-functional groups of the PAC (Fig. S3).

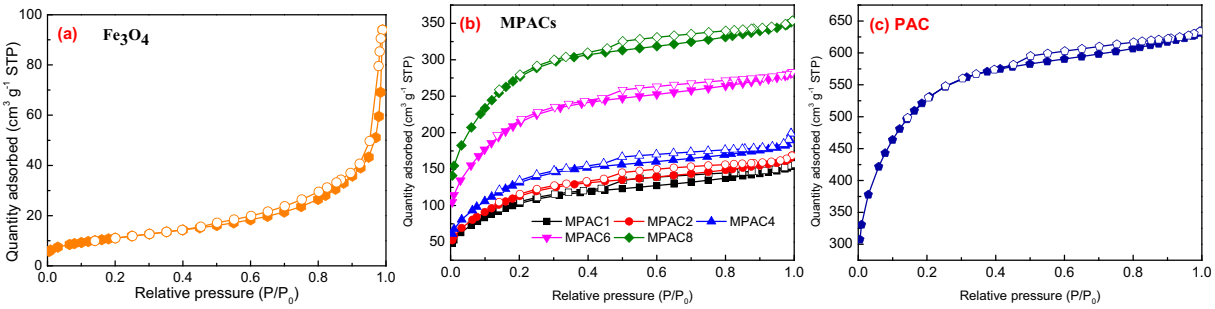

Fig. 1. Nitrogen adsorption–desorption isotherms of (a) Fe_3O_4, (b) MPACs and (c) PAC (solid and empty symbols correspond to the adsorption and desorption).

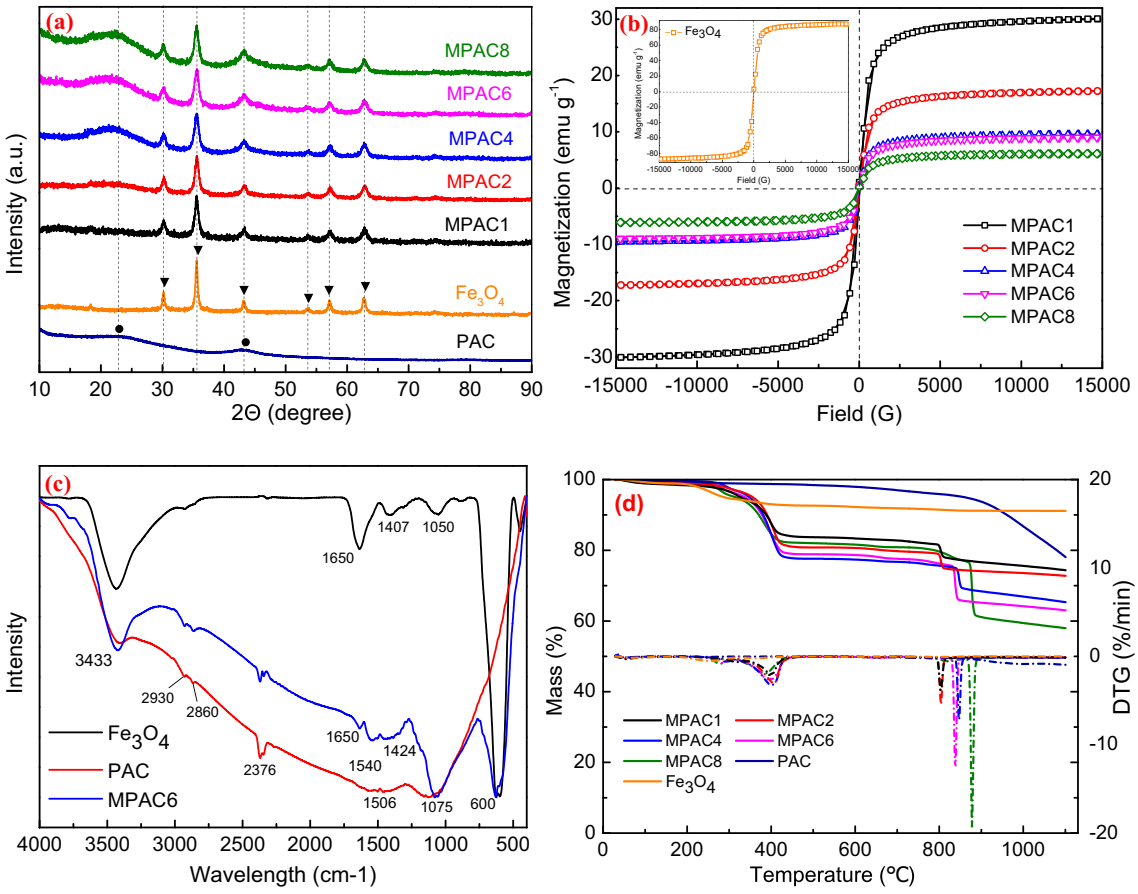

Fig. 2. Characterization of Fe_3O_4, PAC and MPACs: (a) XRD patterns; (b) Hysteresis loop at room temperature; (c) FTIR spectra; (d) TGA analysis.

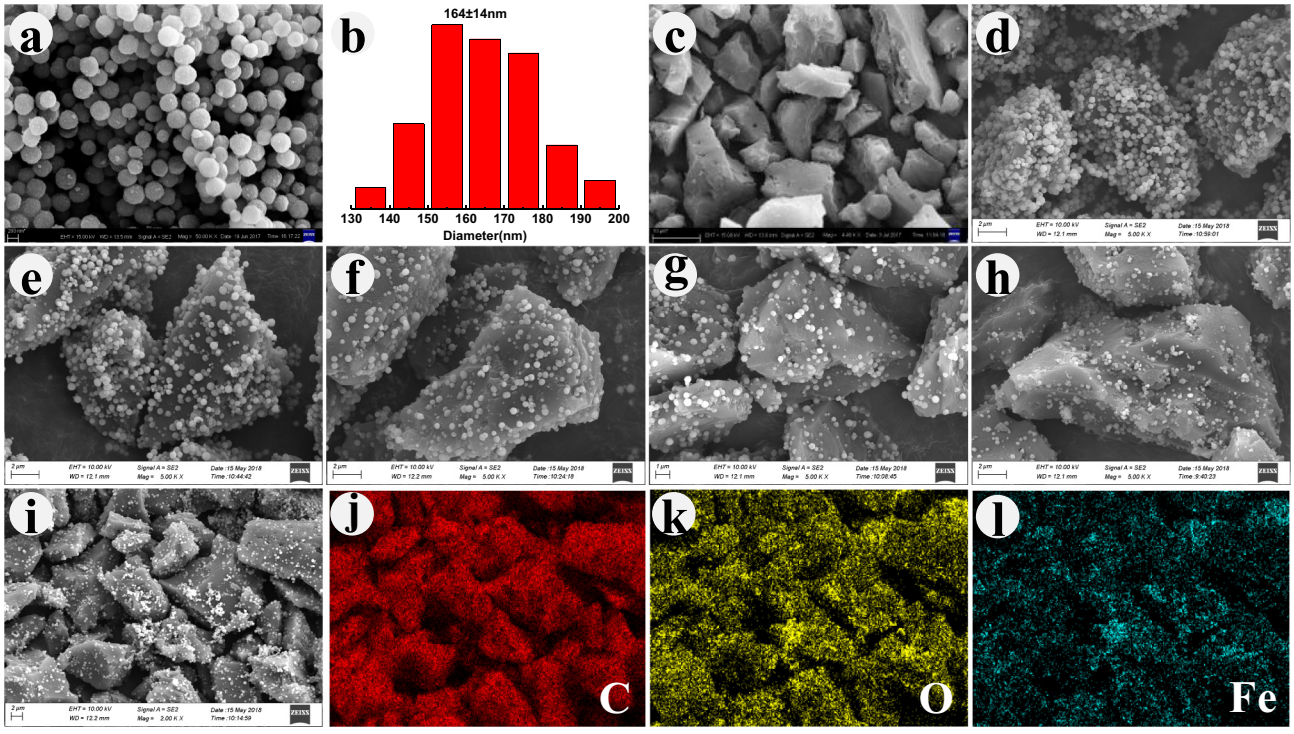

Fig. 3. SEM images of (a) Fe_3O_4, (c) PAC, (d–h) MPAC1, MPAC2, MPAC4, MPAC6, MPAC8 at magnification of 5000 x, (i) MPAC6 at magnification of 2000 x and (j–l) elemental mappings of MPAC6; (b) Particle size distribution of Fe_3O_4.

3.2. Effect of pH on SMX adsorption

Solution pH is an essential variable for adsorption characteristics as it not only affects the surface binding sites of the adsorbents but also the ionization of the adsorbates. As shown in Fig. 4, SMX sorption on the prepared sorbents exhibited a prominent pH dependence, and the largest SMX removal was observed at a pH of 2–4 (>98.6%). π-π electron donor-accepter (EDA) interactions between aromatic pollutants and carbonaceous adsorbents have been frequently mentioned in low pH values, which occurs between two oppositely polarized quadrupoles of benzene rings (Keiluweit and Kleber, 2009; Pan and Xing, 2008). According to the XRD results, MPAC6 can act as a strong π-electron donor due to the presence of π-electron-rich graphene sheets. SMX is recognized as a π-electron acceptor because of the strong electron-withdrawing ability of the sulfonamide group, which could endow the two aromatic rings in SMX with electronic defects (Ji et al., 2011). Also, the protonated amino group ($-NH_3^+$) was proven to improve the electron-accepting ability of SMX^+ (Wang et al., 2019). The main species of SMX were SMX^0 and SMX^+ in the pH range of 2–4, where the distribution fraction of SMX^+ decreased from 33.38% to 0.49% while SMX^0 increased from 66.60% to 97.08% (Fig. S4). The decreased SMX^+ contents at pH 2–4 could lead to a decrease of π-π EDA attractive forces. However, decreased ionization could improve the hydrophobic interactions with the adsorbents (Chen et al., 2017). Thus, the apparent pH influence on the slightly decreased adsorption of SMX at pH 2–4 depended on the increase in hydrophobic interactions counteracts the decrease of π-π EDA interactions. SMX removal gradually decreased from 95.4% to 80.6% as pH increased from 5 to 9, and then quickly declined to 19.5% with a further increase in pH to 12. At a pH of ~5, the SMX^- ratio was about 20%, which increased to over 99% at pH 7.6 and then was essentially constant at higher pH values (Fig. S4). As the pH_{ZPC} (zero point of charge) of MPAC6 was about 5.7 (Fig. S5), MPAC6 was negatively charged when the pH was greater than 6. Therefore, the adsorption reduction observed at pH > 6 was due to the electrostatic repulsion between SMX^- and the negatively charged MPAC6. The SMX removal efficiencies remained in the range of 86.7–80.6% at pH 7–9, which meant that the overall negatively charged MPAC6 was capable of adsorbing SMX^- (Fig. 4). This clear adsorption of SMX^- over this pH range of 7–9 was assumed to be caused by the formation of a negative charge-assisted H-bond, (−)CAHB, or anion exchange. (−)CAHB was strongly demonstrated to form between anionic sulfonamides and O-containing groups (e.g. carboxyl or phenolic hydroxyl) of biochars or CNTS (Teixidó et al., 2011; Li et al., 2013). Here, SMX^- was capable of engaging in H-bonding as H-donor, while the surface oxo-anion of MPAC6 served as H-acceptor. As the (−)CAHB generally derived from the sharing of a proton between H-donor and acceptor with small ΔpKa (≤~4) (Ling et al., 2016; Gilli et al., 2009), the closer pKa (5.6) of SMX and pH_{ZPC} (5.7) of SMX6 further determined this stronger (−)CAHB interaction.

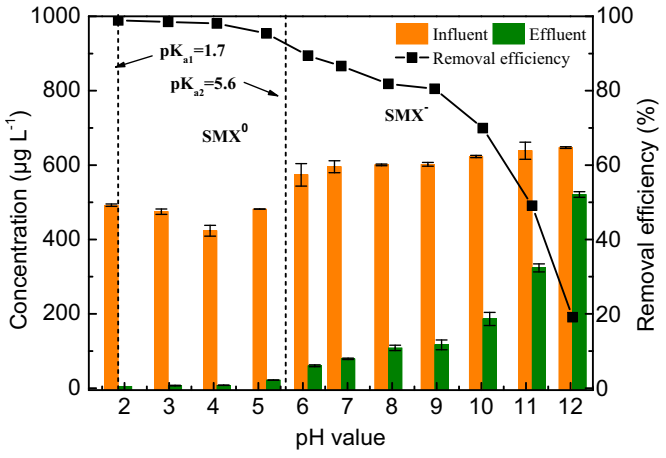

Fig. 4. Effect of initial pH on SMX adsorption onto MPAC6 (Adsorption conditions: m/V = 0.1 g L^{-1}, SMX = 600 μg L^{-1}, pH = 2–12, t = 3 h, T = 25 °C, I = 0.01 M NaCl).

3.3. Effect of co-existing interferents on SMX adsorption

As displayed in Fig. 5a, the effects of ion species (Cl^-, SO_4^{2-}, NO_3^-, PO_4^{3-}, NH_4^+) and strength (0–0.05 M) on the adsorption of SMX on MPAC6 were further investigated. Previous research has shown that ionic strength can suppress anion exchange by electrostatic screening (Li et al., 2013; Peng et al., 2018). The adsorption capacities decreased with the increasing ionic strength of these ion species, which confirmed that anion exchange could be responsible for the SMX^- adsorption on negatively charged MPAC6. Comparing the decreased adsorption capacities with the coexistence of monovalent (Cl^-, NO_3^-), divalent (SO_4^{2-}), and trivalent (PO_4^{3-}) cations, it can be concluded that the inhibition of anions varied from species rather than the amount of charges. The high NO_3^- concentration (0.05 M) showed a pronounced inhibitory effect (41%) on SMX adsorption. There was no significant negative influence (<20%) on the adsorption process at the lowest ionic strength (0.001 M).

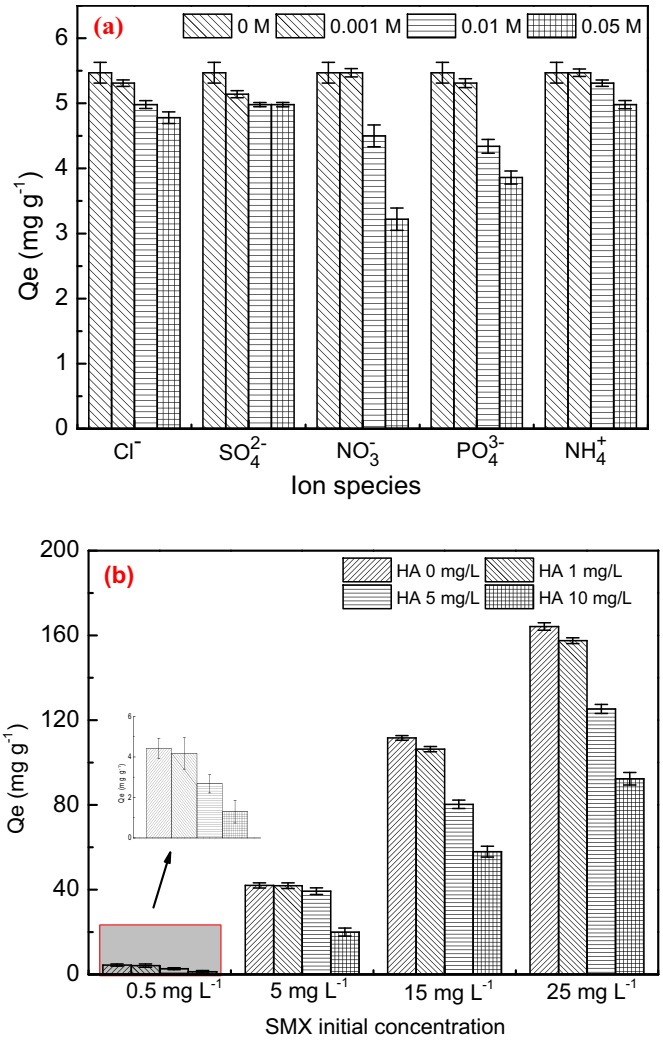

Fig. 5. (a) Effect of ion species and ion strength on SMX adsorption (m/V = 0.1 g L^{-1}, SMX = 0.6 mg L^{-1}, pH = 7, t = 3 h, T = 25 °C, I = 0–0.5 M NaCl, T = 298 K); (b) Effect of humic acid on SMX adsorption onto MPAC6 (m/V = 0.1 g L^{-1}, SMX = 0.5–25 mg L^{-1}, pH = 7, t = 3 h, T = 25 °C, I = 0.01 M NaCl, T = 298 K).

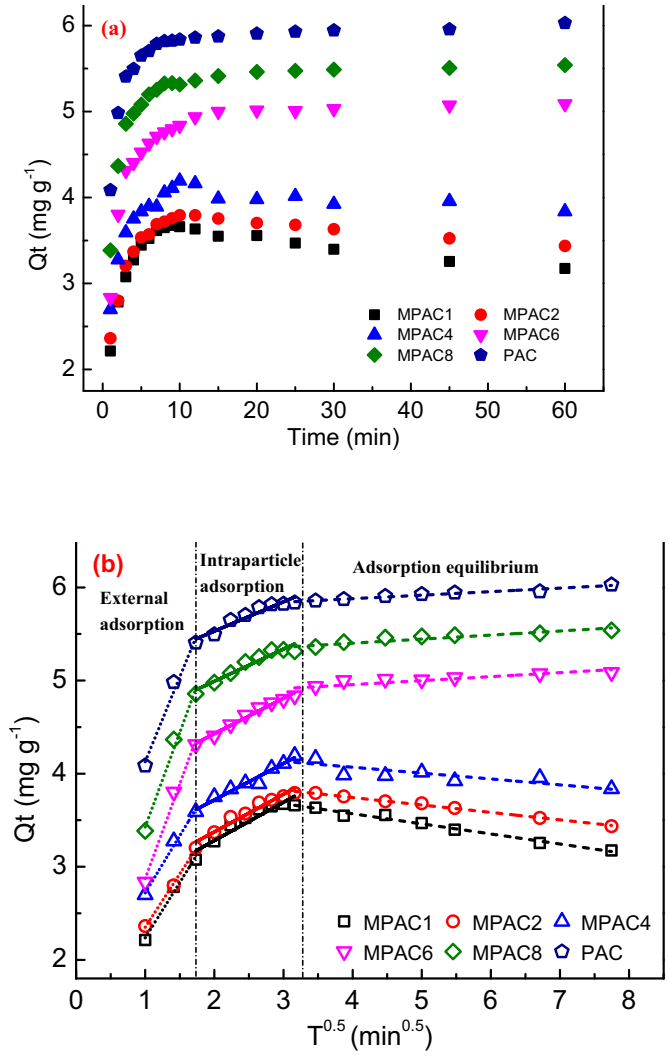

Fig. 6. (a) Adsorption kinetics and (b) intraparticle diffusion model for SMX on MPACs and PAC (m/V = 0.1 g L^{-1}, SMX = 600 μg L^{-1}, pH = 7, t = 3 h, T = 25 °C, I = 0.01 M NaCl).

Humic acid (HA), as one of the typical components of natural organic matter (NOM), was used to investigate the interference of organic matters on SMX adsorption. The adsorption capacities were slightly decreased at the HA concentration of 1 mg L^{-1} (<6.5%), while they were decreased by 44–71% when added with 10 mg L^{-1} HA (Fig. 5b). This might be due to the HA with abundant phenolic and carboxylic group competed with SMX for adsorption sites on the surface of MPAC6. The remaining SMX adsorbed on the surface was attributed to the existence of micropores on MPAC6, which would not have adsorbed organic matter with large molecular sizes.

3.4. Adsorption kinetics

The pseudo-first-order, pseudo-second-order, and Elovich models were analyzed using non-linear expressions to avoid the methodological bias generated by the linearization of the equations (Simonin, 2016). The adsorption kinetics of SMX on PAC and MPACs are shown in Fig. 6a, with the kinetic parameters summarized in Table 2. Rapid adsorption of SMX occurred during the first 5 min, followed by slower adsorption until the adsorption equilibrium conditions were obtained within ~10 min. However, the adsorption capacities of MPAC1, MPAC2, and MPAC4 declined slightly when extending the contact time to 60 min, resulting in a decline in the fit of the lines to the data (R^2 = 0.71–0.86). This decline could have been caused by the grinding off of MPs from the PAC surface during shaking due to the abrasion of MPACs with multilayered stacked MPs, leading to some release of SMX into the solution. For the MPAC6, MPAC8, and PAC materials, the pseudo-second-order model fit the experimental data quite well (R^2 > 0.985), resulting in good agreement between the experimental and calculated adsorption capacities (Table 2). It is worth noting that the correlation coefficients show that the Elovich model does not match the experimental data.

The intraparticle diffusion model was further examined to identify the rate-determining step in the adsorption of SMX. As illustrated in Fig. 6b, the plots were divided into three-linear stages and did not pass through the origin, suggesting multiple mass transfer steps occurred during the adsorption process (Jiang et al., 2017). The first stage with a sharp curve within 3 min was attributed to external adsorption or boundary layer diffusion and surface adsorption, in which SMX was transported through the bulk solution to the external surface of the adsorbents (Zhu et al., 2011b). The slopes of MPAC6, MPAC8, and PAC in this stage were higher than that of MPACs with higher MPs loading contents (>20%). Hereafter, the intraparticle diffusion and inner site adsorption were dominated in the following stages but at a slower rate (Zhu et al., 2018). Detailed diffusion parameters are summarized in Table S2. In this stage, the diffusion rates ($k_{t,2}$) increased slowly and gradually with increasing the contents of MPs on PAC and MPACs, where $k_{t,2}$ varied from 0.32 to 0.41 mg g^{-1} $min^{-0.5}$. The intraparticle diffusion rates increased after the magnetizing impregnation of carbon materials has also been reported in a previous study (Hao et al., 2018). Finally, the equilibrium stage was obtained. It was noteworthy that small MPs loading on MPACs (<15%) could slightly accelerate the adsorption process.

3.5. Adsorption isotherms

The equilibrium concentration data are correlated using four models namely Langmuir, Freundlich, Temkin, and Dubinin-Radushkevich isotherms (Fig. 7a). The fitting parameters calculated from the non-linear expressions based on Eqs. (5)–(8) are summarized in Table 3. As shown in Table 3, the Dubinin-Radushkevich isotherms revealed the best fit to the experimental points for the adsorption of SMX onto PAC and MPACs with very high R^2 values exceeding 0.99. This model is

Table 2
Kinetic parameters for adsorption of SMX onto MPACs and PAC.

Kinetic model	Parameter	Adsorbent					
		MPAC1	MPAC2	MPAC4	MPAC6	MPAC8	PAC
Pseudo-first-order	Qe (mg g^{-1})	3.50	3.65	3.97	4.88	5.35	5.83
	k_1 (min^{-1})	0.868	0.840	0.982	0.755	0.888	1.08
	R^2	0.824	0.864	0.865	0.916	0.931	0.908
Pseudo-second-order	Qe (mg g^{-1})	3.64	3.82	4.14	5.20	5.65	6.09
	k_2 (g mg^{-1} min^{-1})	0.543	0.467	0.512	0.256	0.299	0.367
	R^2	0.713	0.840	0.863	0.990	0.984	0.985
	α ($\times 10^4$ mg g^{-1} min^{-1})	144	6.66	42.6	0.122	1.01	21.1
Elovich	β (g mg^{-1})	5.40	4.23	4.34	2.18	2.40	2.74
	R^2	0.237	0.414	0.441	0.753	0.698	0.680

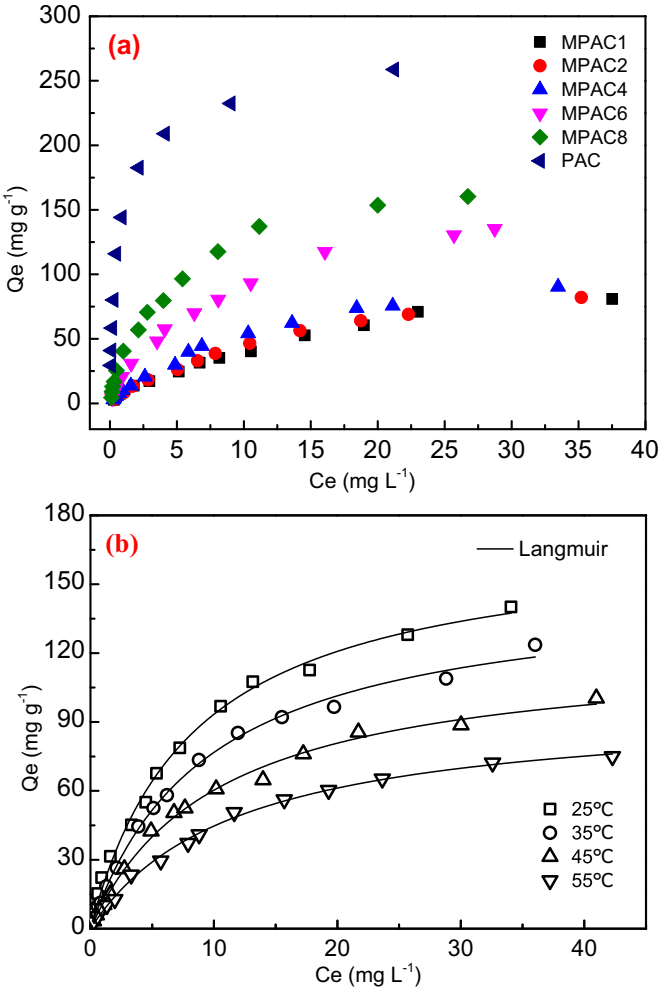

Fig. 7. (a) Adsorption isotherms of SMX on MPACs and PAC and (b) adsorption isotherms on MPAC6 at 25 °C, 35 °C and 45 °C (m/V = 0.1 g L^{-1}, SMX = 0–50 mg L^{-1}, pH = 7, t = 3 h, T = 25 °C/25–55 °C, I = 0.01 M NaCl).

generally applied to express the adsorption mechanism with a Gaussian energy distribution onto a heterogeneous surface (Saadi et al., 2015). The mean free energy (E_{DR}, kJ mol^{-1}) of the adsorption per mole SMX as it is transferred to the surface of the solid from an infinite distance in the solution can be computed by the equation of $E = 1/\sqrt{2K_{DR}}$. The value of E_{DR} in SMX adsorption on PAC was 9.77 kJ mol^{-1} (in the range of 8–16 kJ mol^{-1}), which indicated that the nature of the adsorption process is related to the ion-exchange interactions (Geszke-Moritz and Moritz, 2016). After the addition of the MPs to the PAC, the values of E_{DR} gradually decreased from 9.77 kJ mol^{-1} (PAC) to 6.07 kJ mol^{-1} (MPAC1). The $1/n_F$ values of SMX on MPACs ranged between 0 and 1, indicating favorable adsorption isotherms (Saadi et al., 2015). Based on the Langmuir parameters, the maximum adsorption capacities of SMX on MPACs increased in the order 115 mg g^{-1} (MPAC1) < 119 mg g^{-1} (MPAC2) < 124 mg g^{-1} (MPAC4) < 173 mg g^{-1} (MPAC6) < 183 mg g^{-1} (MPAC8) < 234 mg g^{-1} (PAC). It is noteworthy that Fe_3O_4 has almost no sorption affinity for SMX (Fig. S6). After normalizing based on carbon mass, the adsorption capacities of SMX on MPAC6 and MPAC8 were 214 mg g^{-1} and 222 mg g^{-1}, which was reduced by only 8.8% and 5.1% compared with that on PAC. The decrease in the adsorption capacities of magnetized carbonaceous materials compared with the pristine carbonaceous materials has also been reported in other studies (Reguyal et al., 2017; Mohan et al., 2011). However, the easy recovery of MPACs by the external magnetic field could significantly reduce the treatment cost. In this study, the sharp increase of adsorption capacities was obtained while the MPs were monolayerly deposited on PAC (<20 wt% of Fe_3O_4). Considering these adsorption data, combined with a need for more MPs to achieve good separation, the optimal mass ratio of Fe_3O_4: PAC was concluded to be 1:6, and therefore particles with this ratio were used in subsequent experiments. The adsorption capacity of MPAC6 (173 mg g^{-1}) in this study was relatively good compared to other studies, as they were higher than results using various PACs (94–118 mg g^{-1}) (Teixeira et al., 2019; Calisto et al., 2015), biochars (88–90 mg g^{-1}) (Ahmed et al., 2017; Choi and Kan, 2019), and some magnetic carbonaceous composites (13.8–213 mg g^{-1}) (Table 4) (Heo et al., 2019; Reguyal et al., 2017; Zhang et al., 2020; Reguyal and Sarmah, 2018; Ou et al., 2020). A magnetic $CuZnFe_2O_4$-biochar composite with a higher adsorption capacity of 213 mg g^{-1} was developed by Heo et al. (Heo et al., 2019), but a long time was needed to reach equilibrium than that measured here.

3.6. Thermodynamic studies

Adsorption rates and equilibrium concentrations are a function of temperature changes, and therefore adsorption isotherms of SMX on MPAC6 were obtained for temperatures of 25 °C, 35 °C, 45 °C, and 55 °C. Langmuir equilibrium constants have been frequently reported for ΔG^0 calculations in adsorption studies (Lima et al., 2019). Since the Langmuir isotherm models fit the experimental data well (Fig. 7b), the thermodynamic equilibrium constant (Ka) can be depicted as follows

$$K_a = \frac{1000 K_L M_{adsorbate} [adsorbate]^{\circ}}{\gamma_e} \quad (12)$$

Table 3
Isotherm parameters calculated from nonlinear fitting analysis for SMX adsorption onto MPACs and PAC.

Adsorption model	Parameter	Adsorbent					
		MPAC1	MPAC2	MPAC4	MPAC6	MPAC8	PAC
Langmuir	$Q_{L(max)}$(mg g^{-1})	115 224[a]	119 185[a]	124 167[a]	173 214[a]	183 222[a]	234
	K_L(L mg^{-1})	0.0563	0.0616	0.0765	0.117	0.225	2.07
	R^2	0.994	0.997	0.996	0.994	0.990	0.972
Freundlich	K_F (mg g^{-1})(L mg^{-1})$^{1/n}$	8.61	9.32	11.6	23.0	37.3	133
	1/n	0.667	0.670	0.646	0.595	0.549	0.392
	R^2	0.998	0.996	0.992	0.997	0.995	0.930
Temkin	K_T(dm^3 mg^{-1})	2.40	2.26	2.38	4.08	6.77	21.8
	b_T(J g mol^{-1} mg^{-1})	0.193	0.175	0.152	0.108	0.0919	0.0508
	R^2	0.889	0.898	0.909	0.919	0.943	0.984
Dubinin- Radushkevich	Q_{DAmax}(mg g^{-1})	124	134	150	224	269	437
	K_{DR}($\times 10^{-2}$ mol^2 kJ^{-2})	1.36	1.34	1.28	1.10	0.912	0.524
	E_{DR}(kJ mol^{-1})	6.07	6.10	6.26	6.76	7.40	9.77
	R^2	0.993	0.996	0.996	0.997	0.997	0.995

[a] Expressed on carbon mass basis.

Table 4
Maximum adsorption capacity of SMX onto the adsorbents based on Langmuir isotherms.

Adsorbents	S_{B-E-T} (m^2g^{-1})	SMX concentrations (mg L^{-1})	Adsorption capacity (mg g^{-1})	Reference
Walnut based AC	–	0.5–40	93.5	(Teixeira et al., 2019)
Commercial AC	848	–	118	(Calisto et al., 2015)
Functionalized BC	1.12	0.5–50	88.1	(Ahmed et al., 2017)
Alfalfa-BC	405	10–100	90.0	(Choi and Kan, 2019)
Magnetic pine sawdust BC	126	1–66.2	13.8	(Reguyal et al., 2017)
Magnetic BC	126	0.5–10	19.1	(Reguyal and Sarmah, 2018)
Fe-MIL-88B_NH_2	93.0	20–170	73.5	(Ou et al., 2020)
Magnetic graphited BC	429	10–80	187	(Zhang et al., 2020)
$CuZnFe_2O_4$-BC	61.5	1–80	213	(Heo et al., 2019)
MPAC6	795	0.5–25	173	This study

BC: biochar; AC: activated carbon;

in which $M_{adsorbate}$ is the molecular weight of adsorbate, 253.28 g mol^{-1} for SMX, [adsorbate]° is the standard concentration of the adsorbate, and γ_e is the activity coefficient at the adsorption equilibrium (dimensionless). According to the Debye-Huckel limiting law, γ_e is the function of the ionic strength (I_e) and the charge carried by the solute (Z)

$$\log\gamma_e = -AZ^2I_e^{1/2} \tag{13}$$

According to Eqs. (12)–(13), for neutral or weak charged adsorbates (e.g., organic compounds) (Liu, 2009), the ΔG^0 calculation could be simplified to

$$\Delta G^0 = RT\ln K_a \approx -RT\ln\left[1000K_L M_{adsorbate}\left(1\ mol\ L^{-1}\right)\right] \tag{14}$$

Thermodynamic parameters (ΔG^0, ΔH^0, and ΔS^0) calculated using Eqs. (9)–(11) are summarized in Table S3. The negative value of ΔH^0 (−9.14 KJ mol^{-1}) reflected an exothermic nature of adsorption, and it was consistent with the reduced adsorption capacity with lower temperatures. Basically, the heat evolved during physical adsorption is of the same order of magnitude as the heat of condensation, i.e., 2.1–20.9 kJ mol^{-1} (Liu and Liu, 2008), which indicates that the adsorption of SMX on MPAC6 could be attributed to physical adsorption. The positive value of ΔS^0 (0.055 KJ mol^{-1} K^{-1}) suggested the increase in randomness at the adsorbent-liquid interface during the adsorption of SMX on MPAC6. The negative ΔG^0 indicated that the adsorption process is spontaneous and thermodynamically favorable. Furthermore, the more negative the ΔG^0 is, the larger the driving force for adsorption (Li et al., 2014). The ΔG^0 decreased from −25.6 to −27.2 KJ mol^{-1} with

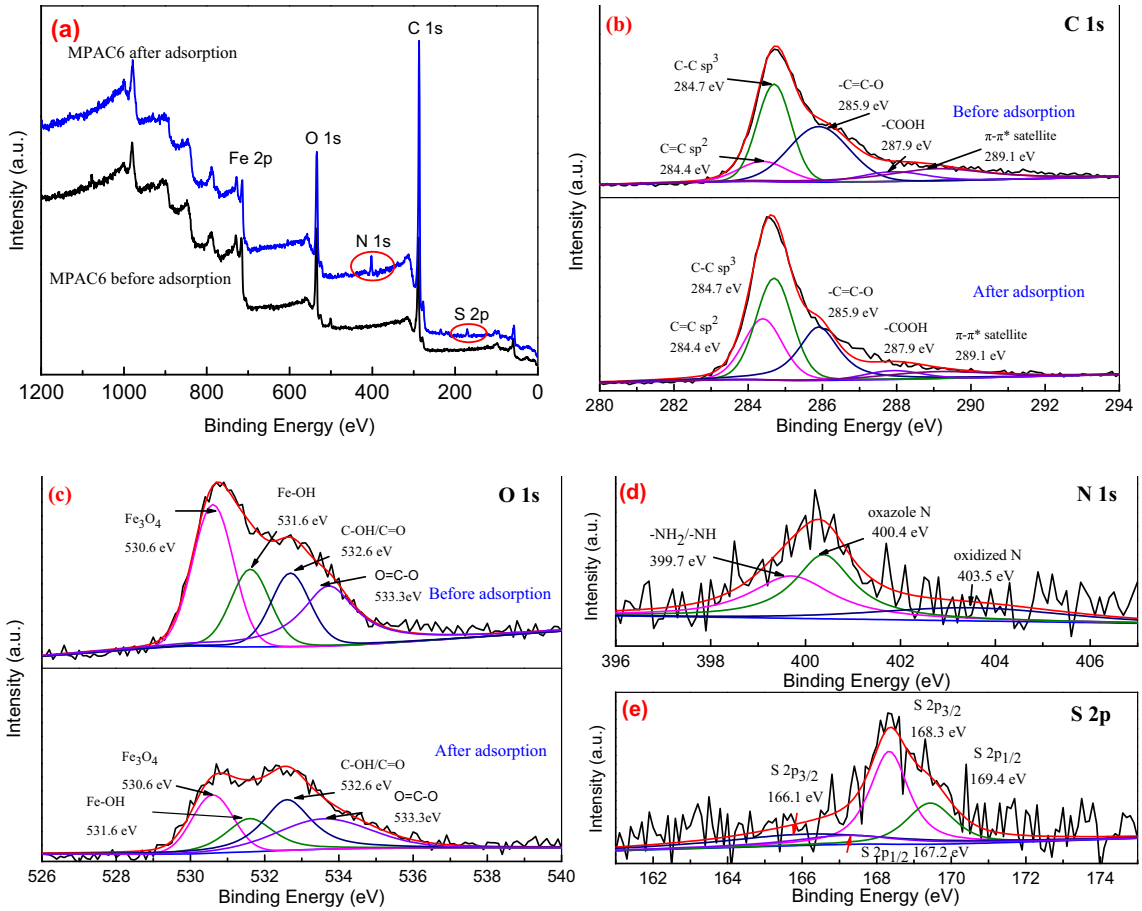

Fig. 8. XPS Spectra of MPAC6 before and after adsorption of SMX (a) full view, (b) C 1 s, (c) O 1 s, (d) N 1 s, and (e) S 2p.

temperature increasing from 25 to 55 °C, which can be attributed to a compromise between the strong driving force and the weakening of the exothermic reaction at higher temperatures.

3.7. Possible adsorption mechanism

The surface structures of MPAC6 before and after adsorption of SMX were compared to further understand the adsorption mechanisms. The full view of XPS spectra (Fig. 8a) showed the presence of nitrogen and sulfur after SMX adsorption, which was consistent with the EDS elemental mapping results as illustrated in Fig. S7. From Fig. 8b, the high-resolution spectrum of C 1s could be deconvoluted into five different peaks at 284.4, 284.7, 285.9, 287.9, and 289.1 eV, assigned to sp^2 C═C, sp^3 C −C, −C═C−O, −COOH and π-π* satellite, respectively (Lan et al., 2016). The presence of abundant sp^2 C═C indicated that π-π stacking could support adsorption of the SMX on MPAC6. The O 1 s spectra could be divided into four characteristic peaks of O species: Fe_3O_4 (530.6 eV), Fe−OH (531.6 eV), C−OH (532.6 eV), and O═C−O (533.3 eV). As displayed in Fig. 8b and Fig. 8c, the oxygen-rich functional groups significantly decreased after SMX adsorption, indicating that the −OH and −COOH groups on the surface of MPAC6 played an important role in the SMX adsorption via hydrogen bonding or Lewis acid-base interaction (Zhang et al., 2020). It was noted that the oxygen content of the MPAC6 decreased from 20.4% to 13.9% after SMX adsorption. The N 1s spectrum of the used MPAC6 suggested the presence of N in oxidized forms besides the $-NH_2$/–NH and oxazole N in SMX (Fig. 8d). The S 2p spectrum displayed four binding energies after SMX adsorption, implying two types of SMX existed in the used MPAC6 while bare SMX exhibited only two binding energies at 168.5 eV (S $2p_{3/2}$) and 169.6 eV (S $2p_{1/2}$) (Lima et al., 2019). Compared with the structure of bare SMX, the variations of the N and S species in the spent MPAC6 could be attributed to the strong interaction between the $-SO_2N^-$– group in SMX and the O-containing groups in MPAC6.

According to the above results, physical adsorption was dominant in the process of SMX adsorption on magnetic carbons. The micro-filling effect facilitated the adsorption of SMX that coexisted with organic matter having molecular sizes. And the adsorption performance of SMX onto MPAC6 was greatly governed by the pH values. The formation of π-π EDA interactions between the aromatic rings of SMX and the MPAC6 with π-electron-rich graphene sheets was responsible for the high adsorption capacities of SMX at pH 2–4. As displayed in Fig. S5, the zeta potentials of the used adsorbents were more positive than those of fresh adsorbents at pH > 8. This could be attributed to the alkalinity consumption by the dissociated protons formed by converting the adsorbed SMX^0 to SMX^- at pH > 8, which implied that the adsorbed SMX on the MPAC6 may exist as its neutral form. The (−)CAHB may occur between SMX^- and the adsorption sites accompanying with the proton exchange of SMX^- with water (Ling et al., 2016). Consistent with the XPS results, the formed (−)CAHB between the $-SO_2N^-$– group in SMX and the O-containing groups in MPAC6 could be considered as the main sorption mechanisms for SMX^- adsorption on magnetic carbons.

3.8. Adsorbents regeneration

The reusability and stability of exhausted adsorbents are essential for the economic application of PACs. According to Fig. S8, ethanol was good for the desorption of SMX and the adsorption capacity of treated adsorbents was 125 mg g^{-1}, which were superior to the application of other desorbent solutions. Considering the properties of SMX, it is more easily dissolved in ethanol than water, with a water solubility of SMX of 0.61 g L^{-1} at 37 °C (Yalkowsky and Dannenfelser, 1992). Thus, the methanol-wash method was efficient. This result also corresponds with a previous finding that the less polar solvents are more suitable for the regeneration of SMX saturated carbonaceous adsorbents, compared to polar solvents (Zhang et al., 2020). However, the solvent

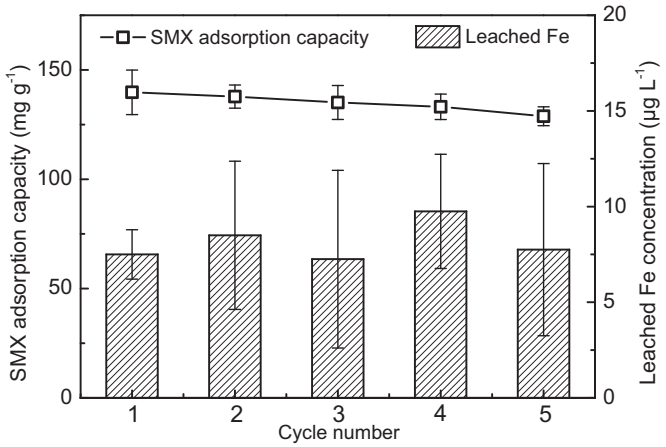

Fig. 9. Adsorption capacity of SMX onto MPAC6 and its stability during five adsorption-thermal reactivation cycles (m/V = 0.1 g L^{-1}, SMX = 25 mg L^{-1}, pH = 7, t = 3 h, T = 25 °C, I = 0.01 M NaCl).

washing methods only transfer the SMX from adsorbents to the liquid phase and cannot eliminate the SMX in situ. Thermal treatment methods have often been reported for the regeneration of the used adsorbents, in which high energy was required to break the chemical bonds (Zeng et al., 2020). The results of five successive adsorption-thermal regeneration cycles (Fig. 9) show that the adsorption capacity of MPAC6 decreased slightly and more than 90% of it was obtained in the 5th cycle. Hence, the thermal oxidation method was chosen for the regeneration of SMX-spent adsorbents in this study. The leaching of Fe elements in the solution was also detected to evaluate the stability of MPAC6. Findings revealed that in all the studied cycles the dissolved iron concentrations were in the range of 5–10 μg L^{-1}, which was far below the permissible limit for drinking water (0.3 mg L^{-1}) determined by WHO (Edition, 2011). The regeneration and reuse of MPAC6 further indicated that the great potential of MPAC6 as an efficient and stable adsorbent for SMX removal.

4. Conclusions

Monolayered MPs were uniformly grown on the surface of PAC using a facile one-pot hydrothermal method. The possible "trade-off" of pore-blocking with magnetic strength of MPACs showed that MPAC6 possessed good Langmuir adsorption capacities for SMX (173 mg g^{-1}) and also excellent magnetic properties (9.0 emu g^{-1}). No significant negative influences were observed on the adsorption process at low ionic strength (0.001 M) of the studied ion species and low concentration of humic acid. The big difference seen among the pH-dependent adsorption was closely related to the speciation of SMX. The cation-assisted electron donor-acceptor interactions (π^+-π) and hydrophobic interaction were responsible for the SMX removal at pHs of 2–4, and (−)CAHB played an important role in the adsorption of hydrophilic SMX^- on negatively charged MPAC6 at neutral or alkaline conditions. The high-efficient magnetic carbon could be obtained with an appropriate Fe_3O_4 loading rate, in which the MPs should be monolayerly grown on PAC with fewer pores blocked and more exposure rate of O-containing groups.

CRediT authorship contribution statement

Miao Lv: Conceptualization, Data curation, Formal analysis, Writing - original draft. **Dongyi Li:** Data curation, Formal analysis. **Zhaohan Zhang:** Supervision, Project administration. **Bruce E. Logan:** Writing - review & editing. **Guohong Liu:** Software, Visualization. **Muchen Sun:** Visualization, Investigation. **Changchao Dai:** Investigation. **Yujie Feng:** Supervision, Project administration.

Declaration of competing interest

The authors declare that they have no known competing financial interests or personal relationships that could have appeared to influence the work reported in this paper.

Acknowledgements

This work was supported by National Key Research and Development Program of China (No. 2016YFC0401106), Heilongjiang Province Natural Science Foundation (No. LH2019E042), and State Key Laboratory of Urban Water Resource and Environment, Harbin Institute of Technology (No. 2019TS06). The authors also acknowledged the support of the Innovation Team in Key Areas of the Ministry of Science and Technology.

Appendix A. Supplementary data

Supplementary data to this article can be found online at https://doi.org/10.1016/j.scitotenv.2020.143717.

References

Ahmed, M.B., Zhou, J.L., Ngo, H.H., Guo, W., Johir, M.A.H., Sornalingam, K., 2017. Single and competitive sorption properties and mechanism of functionalized biochar for removing sulfonamide antibiotics from water. Chem. Eng. J. 311, 348–358.

Altmann, J., Ruhl, A.S., Zietzschmann, F., Jekel, M., 2014. Direct comparison of ozonation and adsorption onto powdered activated carbon for micropollutant removal in advanced wastewater treatment. Water Res. 55, 185–193.

Bao, Y., Lim, T.T., Wang, R., Webster, R.D., Hu, X., 2018. Urea-assisted one-step synthesis of cobalt ferrite impregnated ceramic membrane for sulfamethoxazole degradation via peroxymonosulfate activation. Chem. Eng. J. 343, 737–747.

Calisto, V., Ferreira, C.I.A., Oliveira, J.A.B.P., Otero, M., Esteves, V.I., 2015. Adsorptive removal of pharmaceuticals from water by commercial and waste-based carbons. J. Environ. Manag. 152, 83–90.

Chen, B., Sun, W., Wang, C., Guo, X., 2017. Size-dependent impact of inorganic nanoparticles on sulfamethoxazole adsorption by carbon nanotubes. Chem. Eng. J. 316, 160–170.

Choi, Y.K., Kan, E., 2019. Effects of pyrolysis temperature on the physicochemical properties of alfalfa-derived biochar for the adsorption of bisphenol A and sulfamethoxazole in water. Chemosphere 218, 741–748.

Deng, H., Li, X., Peng, Q., Wang, X., Chen, J., Li, Y., 2005. Monodisperse magnetic single-crystal ferrite microspheres. Angew. Chem. 117, 2842–2845.

Do, M.H., Phan, N.H., Nguyen, T.D., Pham, T.T.S., Nguyen, V.K., Vu, T.T.T., Nguyen, T.K.P., 2011. Activated carbon/Fe_3O_4 nanoparticle composite: fabrication, methyl orange removal and regeneration by hydrogen peroxide. Chemosphere 85, 1269–1276.

Edition, F., 2011. Guidelines for drinking-water quality. WHO chronicle 38, 104–108.

Fan, L., Luo, C., Li, X., Lu, F., Qiu, H., Sun, M., 2012. Fabrication of novel magnetic chitosan grafted with graphene oxide to enhance adsorption properties for methyl blue. J. Hazard. Mater. 215, 272–279.

Gao, P., Mao, D., Luo, Y., Wang, L., Xu, B., Xu, L., 2012. Occurrence of sulfonamide and tetracycline-resistant bacteria and resistance genes in aquaculture environment. Water Res. 46, 2355–2364.

Geszke-Moritz, M., Moritz, M., 2016. Modeling of boldine alkaloid adsorption onto pure and propyl-sulfonic acid-modified mesoporous silicas. A comparative study. Mater. Sci. Eng. C 69, 815–830.

Gilli, P., Pretto, L., Bertolasi, V., Gilli, G., 2009. Predicting hydrogen-bond strengths from acid—base molecular properties. The pKa slide rule: toward the solution of a long-lasting problem. Acc. Chem. Res. 42, 33–44.

Gong, Z., Li, S., Ma, J., Zhang, X., 2016. Self-flocculated powdered activated carbon with different oxidation methods and their influence on adsorption behavior. J. Hazard. Mater. 304, 222–232.

Hao, Z., Wang, C., Yan, Z., Jiang, H., Xu, H., 2018. Magnetic particles modification of coconut shell-derived activated carbon and biochar for effective removal of phenol from water. Chemosphere 211, 962–969.

Heo, J., Yoon, Y., Lee, G., Kim, Y., Han, J., Park, C.M., 2019. Enhanced adsorption of bisphenol A and sulfamethoxazole by a novel magnetic $CuZnFe_2O_4$–biochar composite. Bioresour. Technol. 281, 179–187.

Huang, Y., Ma, E., Zhao, G., 2015. Thermal and structure analysis on reaction mechanisms during the preparation of activated carbon fibers by KOH activation from liquefied wood-based fibers. Ind. Crop. Prod. 69, 447–455.

Ji, L., Wan, Y., Zheng, S., Zhu, D., 2011. Adsorption of tetracycline and Sulfamethoxazole on crop residue-derived ashes: implication for the relative importance of black carbon to soil sorption. Environ. Sci. Technol. 45, 5580–5586.

Jiang, L., Liu, Y., Liu, S., Hu, X., Zeng, G., Hu, X., Liu, S., Liu, S., Huang, B., Li, M., 2017. Fabrication of β-cyclodextrin/poly (l-glutamic acid) supported magnetic graphene oxide and its adsorption behavior for 17β-estradiol. Chem. Eng. J. 308, 597–605.

Joseph, L., Boateng, L.K., Flora, J.R.V., Park, Y.G., Son, A., Badawy, M., Yoon, Y., 2013. Removal of bisphenol A and 17α-ethinyl estradiol by combined coagulation and adsorption using carbon nanomaterials and powdered activated carbon. Sep. Purif. Technol. 107, 37–47.

Kakavandi, B., Jonidi Jafari, A., Rezaei Kalantary, R., Nasseri, S., Esrafili, A., Gholizadeh, A., Azari, A., 2016. Simultaneous adsorption of lead and aniline onto magnetically recoverable carbon: optimization, modeling and mechanism. J. Chem. Technol. Biotechnol. 91, 3000–3010.

Kaur, H., Bansiwal, A., Hippargi, G., Pophali, G.R., 2018. Effect of hydrophobicity of pharmaceuticals and personal care products for adsorption on activated carbon: adsorption isotherms, kinetics and mechanism. Environ. Sci. Pollut. Res. 25, 20473–20485.

Keiluweit, M., Kleber, M., 2009. Molecular-level interactions in soils and sediments: the role of aromatic π-systems. Environ. Sci. Technol. 43, 3421–3429.

Lan, Y.K., Chen, T.C., Tsai, H.J., Wu, H.C., Lin, J.H., Lin, I., Lee, J.F., Chen, C.S., 2016. Adsorption behavior and mechanism of antibiotic sulfamethoxazole on carboxylic-functionalized carbon nanofibers-encapsulated Ni magnetic nanoparticles. Langmuir 32, 9530–9539.

Li, J., Yuan, H., Li, G., Liu, Y., Leng, J., 2010. Cation distribution dependence of magnetic properties of sol–gel prepared $MnFe_2O_4$ spinel ferrite nanoparticles. J. Magn. Magn. Mater. 322, 3396–3400.

Li, X., Pignatello, J.J., Wang, Y., Xing, B., 2013. New insight into adsorption mechanism of Ionizable compounds on carbon nanotubes. Environ. Sci. Technol 47, 8334–8341.

Li, H., Zhang, D., Han, X., Xing, B., 2014. Adsorption of antibiotic ciprofloxacin on carbon nanotubes: pH dependence and thermodynamics. Chemosphere 95, 150–155.

Lima, E.C., Hosseini-Bandegharaei, A., Moreno-Piraján, J.C., Anastopoulos, I., 2019. A critical review of the estimation of the thermodynamic parameters on adsorption equilibria. Wrong use of equilibrium constant in the Van't hoof equation for calculation of thermodynamic parameters of adsorption. J. Mol. Liq. 273, 425–434.

Ling, C., Li, X., Zhang, Z., Liu, F., Deng, Y., Zhang, X., Li, A., He, L., Xing, B., 2016. High adsorption of sulfamethoxazole by an amine-modified polystyrene–divinylbenzene resin and its mechanistic insight. Environ. Sci. Technol. 50, 10015–10023.

Liu, Y., 2009. Is the free energy change of adsorption correctly calculated? J. Chem. Eng. Data 54, 1981–1985.

Liu, Y., Liu, Y.J., 2008. Biosorption isotherms, kinetics and thermodynamics. Sep. Purif. Technol. 61, 229–242.

Liu, Y., Xu, H., 2007. Equilibrium, thermodynamics and mechanisms of Ni^{2+} biosorption by aerobic granules. Biochem. Eng. J. 35, 174–182.

Liu, X., Steele, J.C., Meng, X.Z., 2017a. Usage, residue, and human health risk of antibiotics in Chinese aquaculture: a review. Environ. Pollut. 223, 161–169.

Liu, S., Zhao, H., Lehmler, H.J., Cai, X., Chen, J., 2017b. Antibiotic pollution in marine food webs in Laizhou Bay, North China: trophodynamics and human exposure implication. Environ. Sci. Technol. 51, 2392–2400.

Luo, H., Zhang, S., Li, X., Xu, Q., Liu, J., Wang, Z., 2017. A facile route for preparation of magnetic biomass activated carbon with high performance for removal of dye pollutants. Environ. Sci. Pollut. Res. 24, 15599–15608.

Mohan, D., Sarswat, A., Singh, V.K., Alexandre-Franco, M., Pittman Jr., C.U., 2011. Development of magnetic activated carbon from almond shells for trinitrophenol removal from water. Chem. Eng. J. 172, 1111–1125.

Nguyen, T.D., Phan, N.H., Do, M.H., Ngo, K.T., 2011. Magnetic Fe_2MO_4 (M:Fe, Mn) activated carbons: fabrication, characterization and heterogeneous Fenton oxidation of methyl orange. J. Hazard. Mater. 185, 653–661.

Ou, Y., Yao, L., Li, Y., Bai, C., Luque, R., Peng, G., 2020. Magnetically separable Fe-MIL-88B_NH_2 carbonaceous nanocomposites for efficient removal of sulfamethoxazole from aqueous solutions. J. Colloid Interface Sci. 570, 163–172.

Pamphile, N., Xuejiao, L., Guangwei, Y., Yin, W., 2019. Synthesis of a novel core-shell-structure activated carbon material and its application in sulfamethoxazole adsorption. J. Hazard. Mater. 368, 602–612.

Pan, B., Xing, B., 2008. Adsorption mechanisms of organic chemicals on carbon nanotubes. Environ. Sci. Technol. 42, 9005–9013.

Peng, X., Hu, F., Zhang, T., Qiu, F., Dai, H., 2018. Amine-functionalized magnetic bamboo-based activated carbon adsorptive removal of ciprofloxacin and norfloxacin: a batch and fixed-bed column study. Bioresour. Technol. 249, 924–934.

Ranjithkumar, V., Sangeetha, S., Vairam, S., 2014. Synthesis of magnetic activated carbon/α-Fe2O3 nanocomposite and its application in the removal of acid yellow 17 dye from water. J. Hazard. Mater. 273, 127–135.

Reguyal, F., Sarmah, A.K., 2018. Adsorption of sulfamethoxazole by magnetic biochar: effects of pH, ionic strength, natural organic matter and 17α-ethinylestradiol. Sci. Total Environ. 628, 722–730.

Reguyal, F., Sarmah, A.K., Gao, W., 2017. Synthesis of magnetic biochar from pine sawdust via oxidative hydrolysis of $FeCl_2$ for the removal sulfamethoxazole from aqueous solution. J. Hazard. Mater. 321, 868–878.

Rezaei Kalantary, R., Dehghanifard, E., Mohseni-Bandpi, A., Rezaei, L., Esrafili, A., Kakavandi, B., Azari, A., 2016. Nitrate adsorption by synthetic activated carbon magnetic nanoparticles: kinetics, isotherms and thermodynamic studies. Desalin. Water Treat. 57, 16445–16455.

Rezaei Kalantry, R., Jonidi Jafari, A., Esrafili, A., Kakavandi, B., Gholizadeh, A., Azari, A., 2016. Optimization and evaluation of reactive dye adsorption on magnetic composite of activated carbon and iron oxide. Desalin. Water Treat. 57, 6411–6422.

Saadi, R., Saadi, Z., Fazaeli, R., Fard, N.E., 2015. Monolayer and multilayer adsorption isotherm models for sorption from aqueous media. Korean J. Chem. Eng. 32, 787–799.

Simonin, J.P., 2016. On the comparison of pseudo-first order and pseudo-second order rate laws in the modeling of adsorption kinetics. Chem. Eng. J. 300, 254–263.

Straub, J.O., 2016. Aquatic environmental risk assessment for human use of the old antibiotic sulfamethoxazole in Europe. Environ. Toxicol. Chem. 35, 767–779.

Sun, S., Korheina, D.K., Fu, H., Ge, X., 2020. Chronic exposure to dietary antibiotics affects intestinal health and antibiotic resistance gene abundance in oriental river prawn (Macrobrachium nipponense), and provokes human health risk. Sci. Total Environ. 720, 137478.

Tang, J., Wang, J., 2018. Fenton-like degradation of sulfamethoxazole using Fe-based magnetic nanoparticles embedded into mesoporous carbon hybrid as an efficient catalyst. Chem. Eng. J. 351, 1085–1094.

Teixeira, S., Delerue-Matos, C., Santos, L., 2019. Application of experimental design methodology to optimize antibiotics removal by walnut shell based activated carbon. Sci. Total Environ. 646, 168–176.

Teixidó, M., Pignatello, J.J., Beltrán, J.L., Granados, M., Peccia, J., 2011. Speciation of the ionizable antibiotic sulfamethazine on black carbon (biochar). Environ. Sci. Technol. 45, 10020–10027.

Tong, Y., McNamara, P.J., Mayer, B.K., 2017. Fate and impacts of triclosan, sulfamethoxazole, and 17β-estradiol during nutrient recovery via ion exchange and struvite precipitation. Environ. Sci.: Water Res. Technol. 3, 1109–1119.

Valderrama, C., Gamisans, X., de las Heras, X., Farrán, A., Cortina, J.L., 2008. Sorption kinetics of polycyclic aromatic hydrocarbons removal using granular activated carbon: Intraparticle diffusion coefficients. J. Hazard. Mater. 157, 386–396.

Wan, J., Deng, H., Shi, J., Zhou, L., Su, T., 2014. Synthesized magnetic manganese ferrite nanoparticles on activated carbon for sulfamethoxazole removal. CLEAN–Soil, Air, Water 42, 1199–1207.

Wang, Y., Jiao, W.-B., Wang, J.-T., Liu, G.-F., Cao, H.-L., Lü, J., 2019. Amino-functionalized biomass-derived porous carbons with enhanced aqueous adsorption affinity and sensitivity of sulfonamide antibiotics. Bioresour. Technol. 277, 128–135.

Wei, R., Ge, F., Huang, S., Chen, M., Wang, R., 2011. Occurrence of veterinary antibiotics in animal wastewater and surface water around farms in Jiangsu Province, China. Chemosphere 82, 1408–1414.

Yalkowsky, S.H., Dannenfelser, R.M., 1992. Aquasol database of aqueous solubility, College of Pharmacy, University of Arizona. Tucson, AZ 189.

Yang, W., Yang, W., Kong, L., Song, A., Qin, X., Shao, G., 2018. Phosphorus-doped 3D hierarchical porous carbon for high-performance supercapacitors: a balanced strategy for pore structure and chemical composition. Carbon 127, 557–567.

Zeng, S., Choi, Y.-K., Kan, E., 2020. Iron-activated bermudagrass-derived biochar for adsorption of aqueous sulfamethoxazole: effects of iron impregnation ratio on biochar properties, adsorption, and regeneration. Sci. Total Environ. 141691.

Zhang, G., Qu, J., Liu, H., Cooper, A.T., Wu, R., 2007. $CuFe_2O_4$/activated carbon composite: a novel magnetic adsorbent for the removal of acid orange II and catalytic regeneration. Chemosphere 68, 1058–1066.

Zhang, Q.Q., Ying, G.G., Pan, C.G., Liu, Y.S., Zhao, J.L., 2015. Comprehensive evaluation of antibiotics emission and fate in the river basins of China: source analysis, multimedia modeling, and linkage to bacterial resistance. Environ. Sci. Technol. 49, 6772–6782.

Zhang, D., Luo, Q., Gao, B., Chiang, S.Y.D., Woodward, D., Huang, Q., 2016. Sorption of perfluorooctanoic acid, perfluorooctane sulfonate and perfluoroheptanoic acid on granular activated carbon. Chemosphere 144, 2336–2342.

Zhang, R., Zheng, X., Chen, B., Ma, J., Niu, X., Zhang, D., Lin, Z., Fu, M., Zhou, S., 2020. Enhanced adsorption of sulfamethoxazole from aqueous solution by Fe-impregnated graphited biochar. J. Clean. Prod. 120662.

Zhu, J., Wei, S., Gu, H., Rapole, S.B., Wang, Q., Luo, Z., Haldolaarachchige, N., Young, D.P., Guo, Z., 2011a. One-pot synthesis of magnetic graphene nanocomposites decorated with core@double-shell nanoparticles for fast chromium removal. Environ. Sci. Technol. 46, 977–985.

Zhu, H.Y., Fu, Y.Q., Jiang, R., Jiang, J.H., Xiao, L., Zeng, G.M., Zhao, S.L., Wang, Y., 2011b. Adsorption removal of congo red onto magnetic cellulose/Fe_3O_4/activated carbon composite: equilibrium, kinetic and thermodynamic studies. Chem. Eng. J. 173, 494–502.

Zhu, S., Huang, X., Wang, D., Wang, L., Ma, F., 2018. Enhanced hexavalent chromium removal performance and stabilization by magnetic iron nanoparticles assisted biochar in aqueous solution: mechanisms and application potential. Chemosphere 207, 50–59.

Zietzschmann, F., Aschermann, G., Jekel, M., 2016. Comparing and modeling organic micro-pollutant adsorption onto powdered activated carbon in different drinking waters and WWTP effluents. Water Res. 102, 190–201.